An Experimental Study of Rain Effects on Fine Structures of Wind Waves

ZHIZHANG YANG, SHIH TANG, AND JIN WU*

Air–Sea Interaction Laboratory, Graduate College of Marine Studies, University of Delaware, Lewes, Delaware

(Manuscript received 8 April 1996, in final form 2 August 1996)

ABSTRACT

Previous experiments suggested that rain had dual effects on wind waves: damping in the gravity range and enhancement in the capillary–gravity/capillary range. These results in the frequency domain obtained from fixed-point measurements, however, might be contaminated by the Doppler effect. In the present study, wave slopes were spatially mapped with a scanning laser slope gauge under wind velocities of 3, 5, and 7 m s^{-1} and rain intensities of 42, 68, and 115 mm h^{-1}. Synthesized spectral densities, which are not affected by the Doppler effect, were obtained by processing the data in both ''fixed point'' and ''spatial scan'' modes. The existence of dual effects is clarified with the present results.

1. Introduction

Rain falling on the ocean surface can change the air–sea interaction processes in several ways. When raindrops strike the water surface, they generate ripples (Houk and Green 1976; Poon et al. 1992) and calm down the surface gravity waves (Reynolds 1900; Manton 1973; Tsimplis 1992; Poon et al. 1992). Meanwhile, the rain can enhance the wind stress acting on the sea surface (van Dorn 1953; Caldwell and Elliot 1971, 1972). It also affects the water temperature and salinity in the rain-induced mixed layer immediately below the air–sea interface (Katsaros and Buettner 1969; Green and Houk 1979). More recently, a downpour on the sea surface was claimed as the cause for the echo-free regions of the SAR image (Atlas 1994). Since oceanic remote sensing is governed by sea surface features, there is no doubt that rain may affect the accuracy of radiometric sensing of water temperature and scatterometry retrieval of sea surface winds.

In our previous studies (Poon et al. 1992), dual effects of rain and generation and attenuation of surface waves occurring at different frequencies were suggested to be potentially useful for the detection of rain cells. These results were deduced, however, from single-point measurements, which might be contaminated by the Doppler effect. Our present study is intended not only to clarify this influence, but is also motivated by inconclusive descriptions about the rain influence on the spectral components of surface roughness (Atlas 1994). Spatial measurements of wave slopes under various wind and rain conditions are conducted with a scanning laser slope gauge. These measurements provide unbiased assessments of the rain influence on sea surface roughnesses at various spectral components. A significant spectral enhancement was found in the capillary/capillary–gravity range while damping was observed at dominant wave components. Details of these results are presented herewith.

2. Experiments

a. Experimental setup

1) OVAL TANK

The experiments were conducted in an oval-shaped circulating wind–wave tank, as shown in Fig. 1. The tank consists of two straight sections each 7 m long and two semicircular sections with a centerline radius of 1.35 m. The tank is 31 cm wide and 44.5 cm high. The water depth was maintained at 22 cm during the experiments; tap water was used for all experiments. Wind waves were generated by a variable-speed fan mounted in the back straight section of the tank. All the measurements were performed at the straight section in the front.

2) RAIN MODULES

The rain module was installed at the front straight section of the tank (see Fig. 1); it is a plastic box spanning across the tank, 1 m long and 20 cm high. The

* Additional affiliation: Institute of Hydraulic and Ocean Engineering, National Cheng Kung University, Tainan, Taiwan, Republic of China.

Corresponding author address: Dr. Jin Wu, Air–Sea Interaction Laboratory, Graduate College of Marine Studies, University of Delaware, Lewes, DE 19958.
E-mail: Jin.Wu@mvs.udel.edu

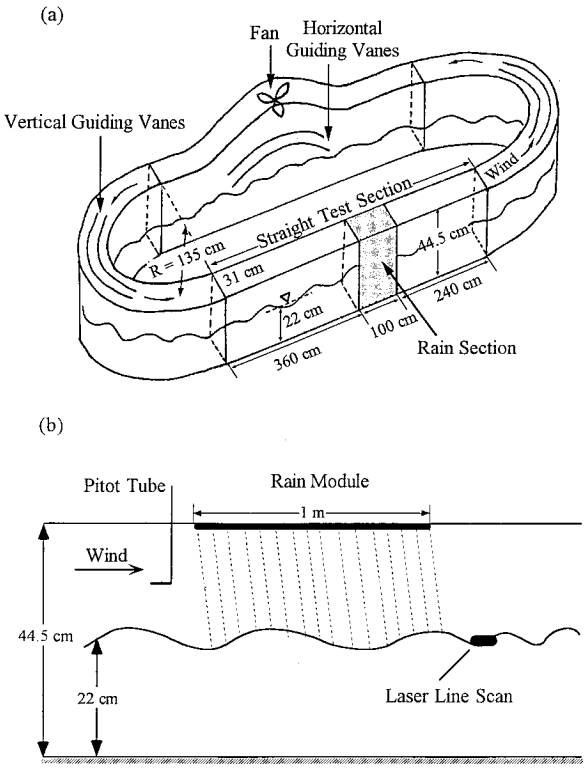

FIG. 1. Circulating wind–wave tank and experimental setup.

upwind end of the rain module was located at 3.6 m downwind from the end of the curve section. Uniformly spaced hypodermic needles, 3 cm apart from their centers, were arranged in a staggered fashion at the bottom of the box. The artificial rain with drops about 2.6 mm in diameter was generated by allowing tap water to flow through hypodermic needles of the gauge number 23. Over a wide range of rain intensity from 2 to 250 mm h^{-1}, raindrop diameters range from 0.5 to 5 mm (Cataneo and Stout 1968; Willis and Tattelman 1989). The present size is about average. In addition, rain intensities were controlled by the water depth in the rain module; the depth was kept constant during each data run.

b. Surface roughness

1) MEASUREMENTS

Sea surface roughness is composed of waves with various scales; its characteristics can be quantified in terms of wave slopes. In this study, the spatial features of wave slopes were measured with a Scanning Laser Slope Gauge (SLSG: Li et al. 1993). The principle of light refraction is used in mapping wave slopes with the SLSG. A 10-mW infrared laser beam at 816-nm wavelength is directed vertically upward; it scans an 8.0-cm line on the mean water surface via a mirrored polygon. After being refracted at the water surface, the laser beam projects onto an image plane placed at the focal distance of a convex lens above the tank. A position sensor is used to track coordinates of the laser spot on the image plane, from which both the upwind–downwind and crosswind slopes can be deduced through Snell's law. The lens focuses all parallel beams toward the same point on the image plane; this thus ensures our slope measurements to be insensitive to the water surface undulation.

During the experiment, the SLSG was aligned to scan in the upwind–downwind direction. The center of the line scan was set at 31 cm away from the downwind edge of the rain module. Each line scan was completed within 1.28 ms; the corresponding scan speed of about 62.5 m s^{-1} was much faster than the phase speed of dominant wind waves. Spatial features of the wave field were thus effectively ''frozen'' during each scan. For each experimental run, a 40-s dataset, which corresponded to 10 000 line scans, was used in the analysis. Along each scan, 64 data points were sampled. The laser beam scanned the same location along its path every 4 ms. Therefore, the SLSG also provided fixed-point slope measurements with the sampling rate of 250 Hz.

2) FREQUENCY SPECTRA

As described above, time series of slopes were obtained at each point in space, while 8192 data points were used in the frequency spectral analysis. These data points were evenly divided into four segments. The data in each segment were first processed through a Hamming window to decrease the spectral leakage (Blackman and Tukey 1958); subsequently a standard fast Fourier transform is applied to these windowed data, while the lost variance due to the windowing is corrected. Following this procedure, a frequency slope spectrum with a frequency resolution of $250/2048 = 0.122$ Hz and degrees of freedom of $4 \times 2 = 8$ was estimated. For each run, time series from the ten points centered at the middle of the scan path were analyzed to obtain ten spectra. To increase the reliability of the spectral estimation, these ten spectra were further averaged; the final spectrum was obtained by averaging every three spectral lines of the averaged spectrum. Overall, the Nyquist frequency of the spectral analysis is $250/2 = 125$ Hz; the frequency resolution is $0.122 \times 3 = 0.366$ Hz. Each spectral component has a $8 \times 10 \times 3 = 240$ degrees of freedom. The frequency spectra thus obtained are biased by the Doppler shift with higher frequency components suffering more. Despite this, frequency slope spectra may still offer some useful results of spectral shapes. For low-frequency components, such as those near the spectral peak, the Doppler frequency shift is negligible. Thus, the spectral estimation from fixed-point measurements is assumed unbiased for dominant gravity waves. More concrete discussions are given in section 3.

3) WAVENUMBER SPECTRA

Since our SLSG scans only a spatial distance of 8 cm, the prewhitening method (Mitsuyasu 1977; Banner et al. 1989) is used to remove the longer wave trend. This is realized by taking the spatial derivative of the slope space series. Let $s(x_i)$ ($i = 0, 1, 2, \cdots, 63$) represent the space series of slopes uniformly distributed along each scan, where the x_i denote the spatial coordinates of sampled data along the scan; their spatial derivatives, $c(x_i)$, are given by

$$c(x_i) = [s(x_{i+1}) - s(x_i)]/(x_{i+1} - x_i), \quad i = 0, 1, \cdots, 62. \tag{1}$$

The above consists of the curvature spatial series. In order to meet the sample size requirement of the Fourier transform algorithm (here 64 data points), $c(x_{63}) = c(x_{62})$ is assumed. Wavenumber spectral analysis is applied to the data from each scan, following the same procedures as those for the frequency spectral analysis. Together, data from 1000 scans, selected every other 10 from the 10 000 subsequent line scans, are used to obtain 1000 raw spectra. The final spectrum determined by averaging over these raw spectra is, in fact, the wavenumber curvature spectral density; the wavenumber slope spectral density is estimated through the division between the square of the wavenumber and the corresponding components in the curvature spectral density. The wavenumber resolution in the spectral estimation is 0.79 rad cm^{-1}, while the ''Nyquist'' wavenumber is 25.13 rad cm^{-1}. Each spectral element has 2000 degrees of freedom.

c. Experimental conditions

The experiments were conducted at wind velocities of $U = 3$, 5, and 7 m s^{-1}. These wind velocities were measured at 11 cm above the mean water surface with a Pitot tube located at 20 cm upwind from the upwind edge of the rain module. Measurements were performed at rain intensities of 0, 42, 68, and 115 mm h^{-1}. The wind was turned on for 15 minutes before any measurements were taken to assure that a steady wind wave field was obtained. Since rainfall may accelerate air and roughen water surface, wind fields in rain area were changed compared with those without rain (Caldwell and Elliott 1971). In the rain section, wind wave growth rate was altered. This is an inseparable part of the rain effect and is involved in the measured results. The Pitot tube in front of the rain region displayed unnoticeable wind variation after the rain was introduced in the wave field. Therefore, it is reasonable to assume that out of the rain region the wind wave generation rate was not affected by rainfall. It is addressed that surface roughness for both rain and no-rain situations was measured at the same location downwind side of rain module. Hence the measured rain effects were solely due to the presence of rain (Poon et al. 1992).

3. Results

a. Mean-square water-surface slopes

Rain effects on the surface roughness are first presented in terms of mean-square water-surface slopes, $\overline{s^2}$, as shown in Fig. 2. For both rain and no-rain conditions, as shown in Fig. 2a, the mean-square slope increases drastically with increasing wind velocities. The rain effects are most obvious at low wind ($U = 3$ m s^{-1}); the effects become less obvious as the wind velocity increases. The decrease of mean-square slope with increasing rain intensity is observed at low wind; this effect is obscured at moderate to high winds.

The rain effect on surface roughness is further presented in Fig. 2b in terms of the roughness production ratio, $(\overline{s^2} - \overline{s_0^2})/\overline{s_0^2}$, with $\overline{s_0^2}$ indicating the mean-square slopes under no-rain conditions. The damping of surface slopes by rain is clearly shown at low wind. At moderate winds, surface slopes are enhanced by rain, while neither significant damping nor enhancement was observed at high winds.

Figure 2c shows the ratio of slopes between crosswind and upwind–downwind components. In the figure, $\overline{s_c^2}$ and $\overline{s_u^2}$ represent the crosswind and upwind–downwind components of mean-square slopes, respectively. It is quite clear that the directional spreading increases with increasing wind speed. No consistent dependence of directional spreading on rain intensities is observed. It is noted that the directional spreading of ripples is widened by rain-generated ring waves. Since the directional spreading of slopes may be restricted in this narrow tank, results of upwind–downwind slopes are presented in the following discussions.

b. Slope spectra

Note that mean-square slopes are contributed by waves of various scales (Wu 1990). In order to identify the rain effect on various spectral components of surface waves, we have attempted to derive unbiased slope spectral densities from our SLSG measurements. As an illustration, results conducted at $U = 3$ m s^{-1} and no-rain condition are presented in Fig. 3.

First of all, the wavenumber slope spectral density, $\Phi(k)$, obtained from the spatial measurements is presented in Fig. 3a, where k is the wavenumber. Since the surface is effectively frozen during each scan, the spectral estimation in the range of 0.79–25.13 rad cm^{-1} is unbiased. The frequency slope spectral density, $S(f)$, obtained from the fixed-point measurements is shown in Fig. 3b, where f is the frequency. This spectral density covers 0.122–125 Hz, the corresponding wavenumber range is 0.05–20 rad cm^{-1}. The Doppler frequency shift is least significant at low frequencies. Doppler frequency shifts, at various wind velocities, were calculated from $\Delta = kU_d$, where U_d is the wind drift current obtained earlier in the same tank (Tang and Wu 1992). It

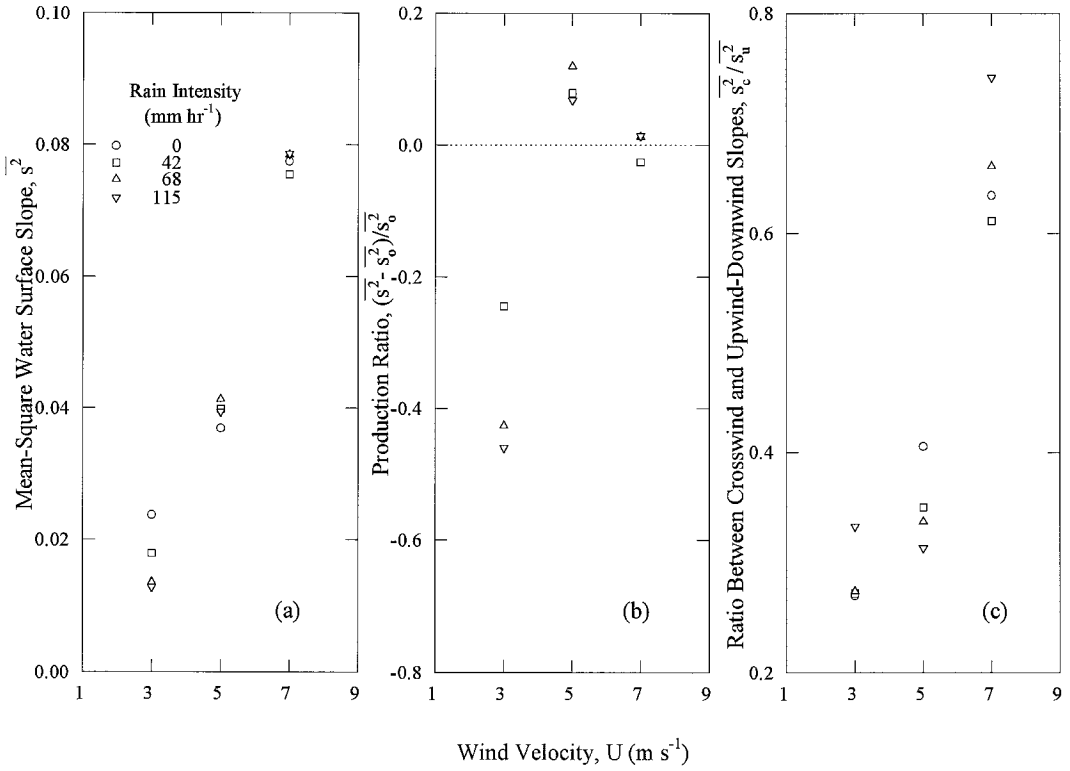

FIG. 2. Properties of mean-square water surface slopes.

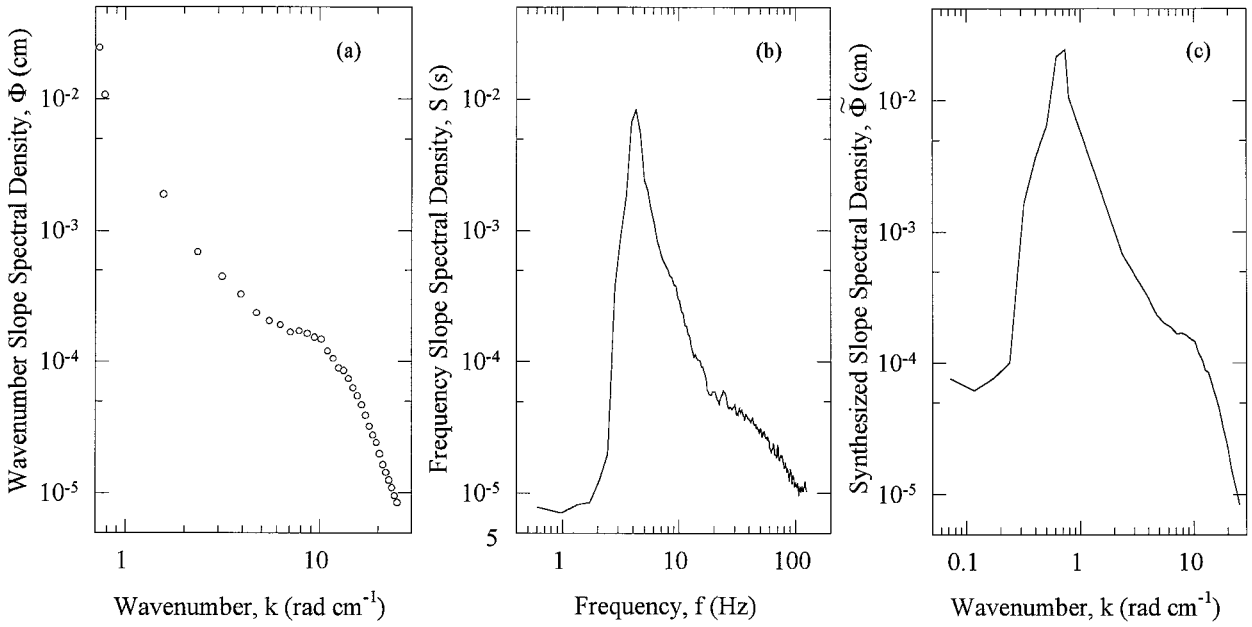

FIG. 3. Procedures to obtain synthesized spectrum. The measurements were performed at a wind speed of 3 m s^{-1} and no-rain condition.

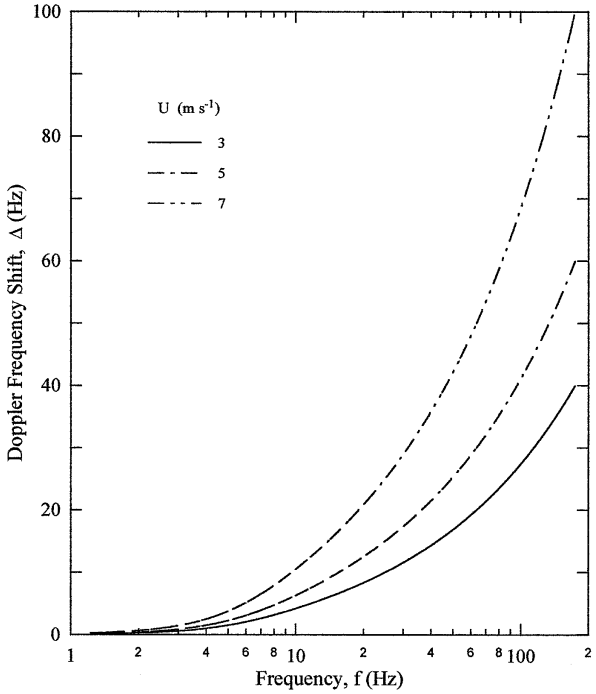

FIG. 4. Doppler frequency shifts at various wind velocities.

is readily seen in Fig. 4 that the Doppler frequency shift is negligible for wave components with $f < 2.5$ Hz.

The unbiased spectrum, as shown in Fig. 3c, is synthesized by letting

$$\tilde{\Phi}(k) = \begin{cases} S(f)(df/dk), & k < 0.79 \text{ rad cm}^{-1} \\ \Phi(k), & k > 0.79 \text{ rad cm}^{-1}, \end{cases} \quad (2)$$

where df/dk can be derived from the surface wave dispersion relation $4\pi^2 f^2 = gk + Tk^3/\rho$ in which g is the gravitational acceleration, T the surface tension, and ρ the water density.

Following this procedure, the unbiased wavenumber spectra for all the experimental conditions are determined, as shown in Fig. 5. Our previous studies (Poon et al. 1992) indicated that there existed different rain effects in gravity and capillary–gravity/capillary regimes. In the following, rain effects in these regimes are discussed separately.

1) GRAVITY REGIME

As shown in Fig. 5, rain effects on surface waves in the gravity regime ($k < 1.56$ rad cm^{-1}) are most obvious at low wind. They are obscured as the wind velocity increases. At low wind, slope spectral densities near the spectral peak are seen in Fig. 5a to be severely damped. The damping effect is enhanced with the increasing rain intensity. The trend is the same as the mean-square slopes at low wind (Fig. 2a). This indicates that the overall roughness in terms of the mean-square slopes is mainly contributed by gravity waves (Wu 1990). Since components near the spectral peak account for the major part of gravity waves, the damping of mean-square slopes results from the suppression of gravity waves. At moderate wind ($U = 5$ m s^{-1}), the damping effects are shown on the high wavenumber side of the spectral peak. Furthermore, there is also a slight enhancement for components on the low wavenumber side. Generally speaking, this phenomenon becomes more obvious with increasing rain intensity. This may be attributed to a

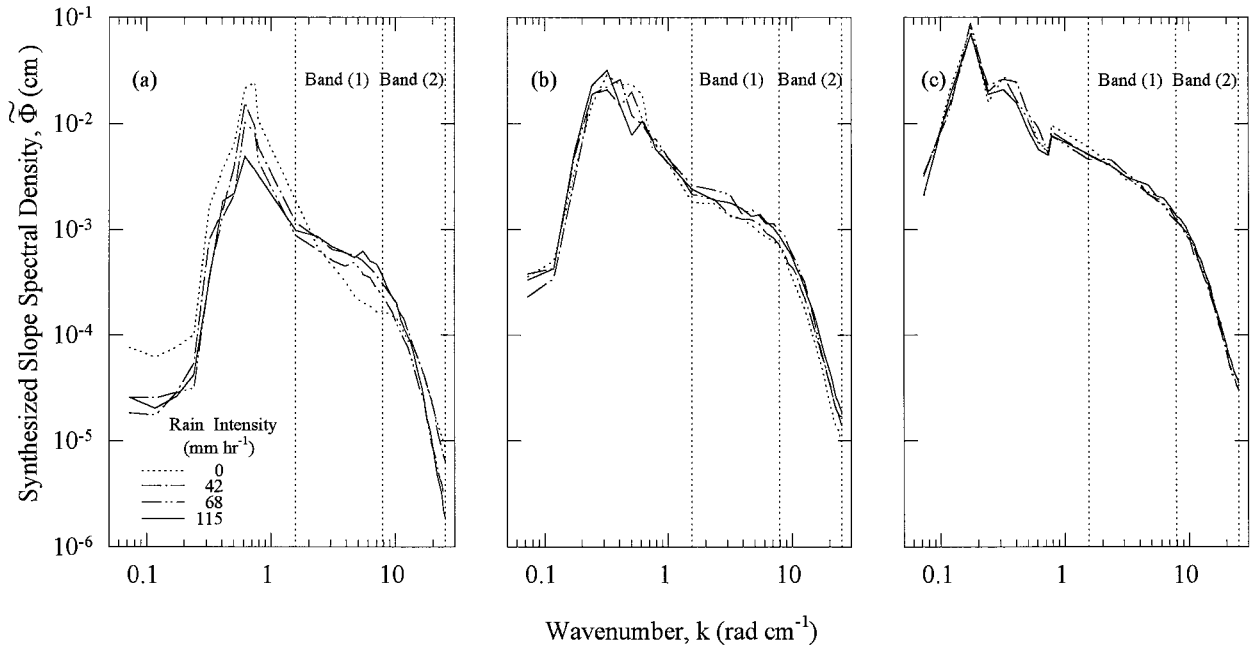

FIG. 5. Synthesized wavenumber slope spectral densities at wind velocities of (a) 3, (b) 5, and (c) 7 m s^{-1}.

greater rain-induced stress from the rain of a higher intensity. The added surface stress is mainly caused by the horizontal velocity components of raindrops impinging on the sea surface (Caldwell and Elliott 1972). These results are not shown in Fig. 2b. It indicates that the high-wavenumber waves contribute more to the roughness at higher winds. At high wind ($U = 7$ m s^{-1}), there are no obvious changes in spectra, suggesting that the wind forcing dominates the generation of surface roughness under this condition.

2) CAPILLARY–GRAVITY/CAPILLARY REGIME

The slope spectra in capillary–gravity/capillary regime in the range of 1.56–25.13 rad cm^{-1} are also shown in Fig. 5. Similar to gravity waves, the rain effects are most significant at low wind; they are less obvious as the wind velocity increases. At each wind velocity, the rain effects also show subtle differences among various rain intensities. Based on the difference in the slope of spectral shape, spectra may be divided into two wavenumber bands, that is, 1) 1.56–7.85 rad cm^{-1}, and 2) 7.85–25.13 rad cm^{-1}. The slope of the spectral shape in band 1 is less steep than that in band 2.

Rain effects on surface waves in these two bands are quite different. At low wind, rain enhances spectral values in band 1 but slightly damps the components in band 2 (see Fig. 5a). Intensities of both enhancement and damping do not vary monotonically with the rain intensity. It should be noted that the coexistence of damping and enhancement in the capillary–gravity/capillary regime was not reported by the earlier measurements (Poon et al. 1992). Poon et al. (1992) recognized that rain damped gravity waves and enhanced capillary–gravity/capillary waves, but they failed to observe its damping effect on the capillary–gravity/capillary waves. Note that fixed-point measurements by Poon et al. (1992) may introduce severe Doppler effects in their measured slope spectra. Due to the oscillating nature of the orbital velocities involved in the long gravity waves, there appears to be a smearing effect in the biased spectra (Hara et al. 1994). In the Poon et al. (1992) results, this nonenhancement smearing effect on the spectral density at high frequencies shadows the damping effects of rain. At moderate wind, waves in both bands are enhanced, and the rain effect is quite obscured at high wind. These are qualitatively consistent with Poon et al.'s (1992) results.

4. Discussion

a. Dual effects

Most of the reported results were derived from experiments in a rain–mechanical wave system (e.g., Caldwell and Elliott 1971; Tsimplis and Thorpe 1989); Poon et al. (1992) conducted the experiment in a rain–wind wave system; they first identified dual effects of rain on

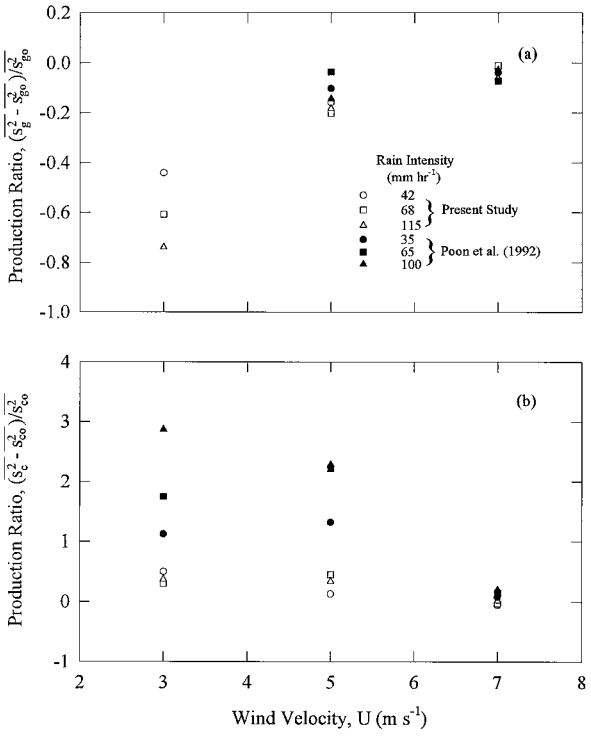

FIG. 6. Rain effects on surface roughness in (a) gravity and (b) capillary–gravity regimes.

wind waves. In this experiment, we again observed the dual effects. Both sets of results are shown in Fig. 6. In Fig. 6a, $\overline{s_g^2}$ and $\overline{s_{go}^2}$ represent the integrated slope spectra over gravity regimes in the situations with and without rain, respectively. In Fig. 6b, $\overline{s_c^2}$ and $\overline{s_{co}^2}$ denote the counterparts in the capillary regime. Besides, we discovered more subtle patterns: dual effects also exist, respectively, in gravity and capillary–gravity/capillary regions at low wind speed, as shown in bands 1 and 2 in Fig. 5a. They vary with both wind speed and rain intensity. Since rain effects show a selective influence at a given wavenumber regime, as described in the previous section, it seems reasonable to discuss the implied mechanisms in terms of spectral regimes.

1) GRAVITY WAVES

As shown in Fig. 5, slopes at spectral peaks and even higher frequencies are damped for all cases investigated. This effect becomes less obvious as the wind velocity increases. Slopes contributed by spectral components at frequencies lower than those at the spectral peak are obviously damped only at low wind. They are slightly enhanced at moderate wind, while there is no observable variation at high wind. We speculate that these spectral behaviors result from the balance between raindrops damping on the gravity waves and work done by the rain stress (Tsimplis and Thorpe 1989; Le Méhauté and Khangaonkar 1990; Poon et al. 1992; Atlas 1994). Rain-

TABLE 1. Momentum fluxes at various experimental conditions.

Wind speed U (m s^{-1})	Rain intensity I (mm h^{-1})	Rain-induced horizontal stress τ (N m^{-2})	Vertical momentum flux M (N m^{-2})
3	42	0.0052	0.0209
	68	0.0088	0.0338
	115	0.0137	0.0572
5	42	0.0083	0.0209
	68	0.0142	0.0338
	115	0.0221	0.0572
7	42	0.0141	0.0209
	68	0.0239	0.0338
	115	0.0374	0.0572

drops may produce both normal and tangential stresses on the water surface when they strike the moving water surface (Le Méhauté and Khangaonkar 1990; Poon et al. 1992). Assuming that horizontal and vertical components of the raindrop impact velocity are U_i and W_i, respectively, the tangential stress can be expressed as $\tau = \rho U_i I$, while the normal stress may be characterized as the vertical momentum flux, $M = \rho W_i I$ (Caldwell and Elliott 1971; Poon et al. 1992). Using the same method as provided by Poon et al. (1992), we obtained that U_i were 0.44, 0.75, and 1.17 m s^{-1} at wind speeds 3, 5, and 7 m s^{-1}, while W_i were 1.79 m s^{-1} regardless of wind speed. Magnitudes of both M and τ under various conditions of this experiment are summarized in Table 1. The tangential stress induces mean currents and enhances gravity waves. The normal stress produces the pressure on the advancing waves and enhances turbulent dissipation of gravity waves, which introduces the damping of gravity waves. As a result, the evolution of gravity waves is affected. We think that these are the dominant mechanisms controlling the net rain effect in the gravity regime. For a given rain intensity, the tangential rain-induced stress τ increases with the increasing wind velocity. Generally speaking, at each rain intensity the value of τ under high wind is approximately two times larger than that at low windspeed; see Table 1. The damping effect is proportional to the vertical momentum flux, $M = \rho W_i I$ (Poon et al. 1992). Since W_i is constant, the vertical momentum flux is determined by rain intensity I. As shown in Table 1, M increases with I. The magnitude of M at the highest rain intensity is almost three times as large as that at the lowest rain intensity. Thus, there is no doubt that gravity waves are most heavily damped at the highest rain intensity. This accounts for the increase of damping at the spectral peak. At low wind speed, the wave dissipation due to the vertical momentum flux dominates the enhancement from tangential rain-induced stress. This results in the damping at the spectral peak; see Fig. 5a. At medium wind (see Fig. 5b), like those at low wind, the spectral peaks are damped. This effect becomes more significant with increasing rain intensity. It is probably due to the dissipation from the vertical momentum flux of rain. Note that the rain-induced tangential stress increases with the wind velocity. This accounts for the downshift of the spectral peaks to lower wavenumbers as well as the enhancement of spectra. The slight enhancement of components at the forward face of the original spectral peaks indicates that at that spectral range, the effect of rain-induced tangential stress overrides the wave damping by rain. There is no doubt that the interacting processes in a rain–wind wave system is quite complex, but it seems that these factors play the dominant roles.

Dominant wavelengths in the present study are about 7.5, 16, and 32 cm at wind speed 3, 5, and 7 m s^{-1}, respectively; see Fig. 5. Approximately, there are 3 to 13 waves under the rain section from low to high winds. Raindrops generate capillary/capillary–gravity waves that subsequently interact with the gravity wind waves in the rain area. Note that the energy exchange between gravity waves and capillaries mainly occurs on the length scale of one gravity wavelength (Zhang 1995), which is much shorter than the length of present rain section. Also, initiation of the rain-induced ripples enhances surface roughness in the rain region and may increase the momentum transfer to the wave field from airflow (Caldwell and Elliott 1972). These processes couple with rain-induced turbulence dissipation. The net effects accumulate as waves pass through rain region and result in the damping on gravity waves. It is noted that the accumulative effect would be more obvious under a longer rain section. However, the damping effect with respect to length of the rain section is usually scaled with a damping coefficient, Δ (Tsimplis 1992; Poon et al. 1992). It represents a spatial damping rate due to rain–wave interaction. Based on Poon et al. (1992), Δ is defined as

$$E_g = E_{go} e^{-\Delta L}, \tag{3}$$

where E_g and E_{go} are, respectively, the integrated square root of spectral densities over gravity regime with and without rain. As indicated in (3), Δ denotes the integrated damping rate of gravity waves. The estimated Δ are shown in Fig. 7. The spatial damping rate decreases with increasing wind velocity. This is consistent with previously reported results (Poon et al. 1992). At low wind ($U = 3$ m s^{-1}), it increases with increasing rain intensity, while at moderate and high wind this trend is blurred.

Meanwhile, it is noted that Doppler effects on the wave components near spectral peaks are negligible (Phillips 1977); see Fig. 4. Hence, the duration of gravity waves remaining within the rain region should not be decreased by the presence of rain-induced surface drift currents.

It is addressed that the vertical component of raindrop impact velocity in the present study is 1.79 m s^{-1}, while that in nature is 7.45 m s^{-1} for a raindrop of the same diameter (Dingle and Lee 1972). The lower impact velocity may result in underestimation of the damping

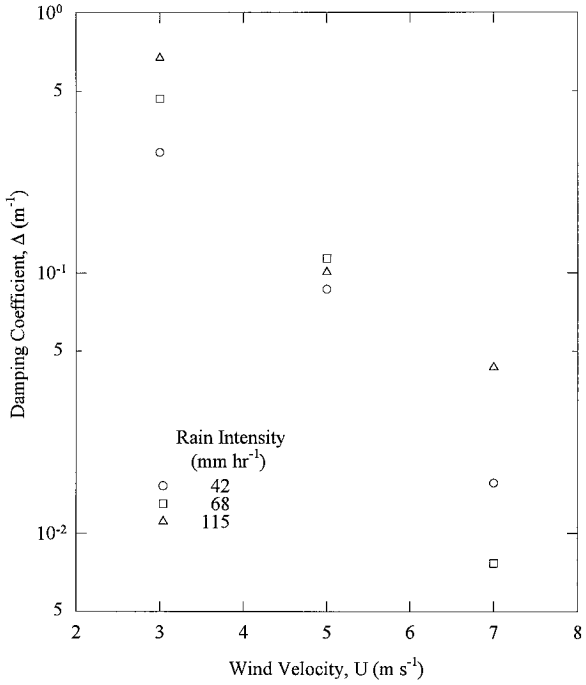

FIG. 7. Damping coefficients in gravity regime.

effect. However, vertical momentum fluxes, which account for the damping effects, are comparable to those in nature due to high rain intensity being used in the present setup. Typical intensities for ordinary and heavy rain in nature are 3.6 and 42.9 mm h^{-1}, respectively (Willis and Tattelman 1989). For a rainfall of the average intensity, 23.5 mm h^{-1} and drop size of 2.6 mm in diameter, the resultant vertical momentum flux is 0.0486 N m^{-2}. It is covered by the present simulation. In spite of this, it is noted that the present study provides a lower boundary of damping effects.

2) CAPILLARY–GRAVITY/CAPILLARY WAVES

Capillary–gravity/capillary waves are usually referred to as ripples. In a wind–wave system, they are generated by the wind stress, gravity waves of large curvature in crests, and wave breaking (Wu 1977). In the presence of rain, ripples may also be generated by raindrops and convected downstream by wind-induced currents and long waves (Poon et al. 1992). Interactions between currents and waves, as well as those between various wave components, play important roles in affecting slopes contributed by ripples. During this experiment, no wave breaking was observed, so the measured ripples were generated by the wind stress, gravity waves, and raindrops.

As shown in Fig. 5, the slope of the spectral shape shows some difference between bands 1, 1.56–7.85 rad cm^{-1}, and 2, 7.85–25.13 rad cm^{-1}. For all cases, the slope in band 1 is smaller than that in band 2. This indicates that in these two regimes, degrees of the spectral saturation are different and thus various mechanisms are related with rain effects (Phillips 1977).

Le Méhauté (1988) quantified analytically capillaries generated by the impact of individual water drops on an initially quiescent water body. It is shown that prevailing waves were in a mixed capillary–gravity regime around a wavenumber k_m = 8.98 rad cm^{-1}, which corresponds to the minimum value of the group velocity. At a short distance from the impact point, the superk_m ($k > k_m$) components have a relatively large amplitude and hide the subk_m components. At large distances, the superk_m components are damped rapidly and only the subk_m are visible. For the present setup, constituents of rain-generated ripples can be traced from the spectra at low wind (Poon et al. 1992). The capillaries are composed of wave components in a wavenumber band approximately between 2.0 and 10.0 rad cm^{-1}; see Fig. 5. The average wavenumber is about 6.0 rad cm^{-1}, which is smaller than k_m. These discrepancies may result from the differences in rain properties between the present setup and the assumption in Le Méhauté (1988): Capillaries are from multiraindrops instead of a single one, while the impact velocity is much less than the terminal velocity. No distinguishable low-frequency (in the subk_m regime) rain-induced ripples were observed since they were masked by the wind-generated ripples (Poon et al. 1992).

In the absence of rain, the spectrum shows a ''dip'' at wavenumbers 3–8 rad cm^{-1} at low wind speed; see Fig. 5a. A steep decrease of spectral densities is observed for wavenumber components beyond the spectral dip. For situations without rain, the dip is gradually filled with an increasing wind. This is consistent with Zhang's (1994) results, where it was indicated that the dip was formed by current–wave instability, which blocked both capillary–gravity waves and parasitic capillaries. He attributed the filling up of the dip as a result of increasing nonlinear interactions and the growth of waves. As shown in Fig. 5a, the present experiment also indicates that rain tends to fill up the dip. This means that the rain may enhance wave growth at low wind speed. The effect of raindrops on the wave growth may be attributed to their roles in the enhancement of the rain-induced stress, wind stress, and nonlinear interaction.

The rain-induced horizontal stress has been discussed above. Raindrops directly generate capillary waves. Ubiquitous capillary waves in the rain region act as roughness elements on the water surface (Wu 1986). This rain-induced roughness enhances the wind stress, thus providing the momentum input from wind to waves, and the wave growth. From the point of view of wave–wave nonlinear interaction, the filling up of the dip may result from the enhanced wave–wave interactions by the introduction of the raindrop-induced capillary waves. The raindrop-induced capillary waves distribute uniformly along the profile of wind waves propagating through the rain region. Undoubtedly, they

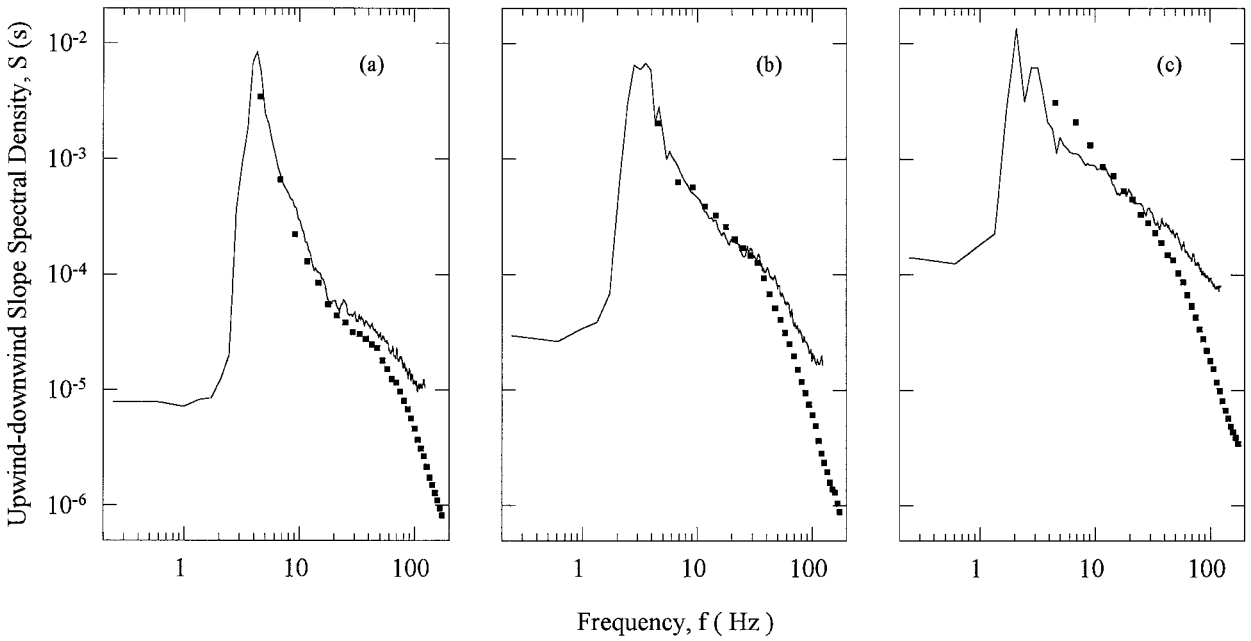

FIG. 8. Frequency spectra from biased (■) and unbiased (–) measurements. The results correspond to no-rain situations.

interact significantly with other wave components to enhance the momentum transfer among various waves. In fact, the filling-up of the dip seems to confirm this. This fact further indicates that capillary waves are of significant dynamical sense in the wave development. Another point that should be noted is that the transition wavenumber between bands 1 and 2 is about 8 rad cm^{-1}. This coincides with the transition wavenumber from the dip to the steep decay on the spectrum at low wind speed. We speculate that the existence of the transition wavenumber results from the same dynamic mechanism as the dip. At moderate wind speed, though rain enhances the spectral components in both bands, the spectral slopes as shown in Fig. 5b remain unchanged. This indicates that the rain does not change the basic dynamic pattern resulting in the spectral saturation in these two bands. At high wind velocity, no rain effects are observed; see Fig. 5c. According to Poon et al. (1992), ripples at high wind speed are mainly generated by gravity waves instead of rain. This masked the rain effects on surface roughness.

It is noted that mean wind speeds in the present study are relatively small compared with those in case of a hurricane. At extremely high winds, horizontal stress may exceed the vertical momentum flux due to the large incident angles of raindrops. We speculate that the surface slope may be enhanced by rain. On the other hand, large- and small-scale wave breaking would be ubiquitous. Gravity waves are vigorously dissipated, while ripples are further enhanced. The resultant effects are beyond the present discussion and should be clarified with further experiments.

b. Frequency shift

The Doppler effect on ripples due to wind-induced drift currents and orbital velocities of long waves has been realized and investigated (Wu 1975). Though a correction method was worked out and proved to be valid, it seems still beneficial to compare the biased and unbiased measurements for understanding the magnitude and mechanism of the Doppler effect. Besides, from the points of view of both rain–wave dynamics and radar remote sensing of rainfall, study of the relation between rain intensity and the Doppler effect is of significance.

Slope spectra from biased fixed-point measurements and those from unbiased spatial measurements are compared in Fig. 8. The spectra were measured at various wind conditions without rain. For a given wind velocity, the difference between the biased and unbiased spectra indicates the magnitude of Doppler effects; the effects become more serious as the wind speed increases. Obviously, this is due to wind-induced drift currents and orbital motions of long waves, which are of larger magnitude at higher wind speed (Wu 1975). But the Doppler effect does not increase monotonically with the increasing frequency. This is due to the oscillating nature of orbital motions involved in long gravity waves. In fact, a transition frequency exists at about 19.6 Hz where the Doppler effect is smeared. At low and moderate winds, the Doppler effect at frequencies lower than the transition frequency is seen in Figs. 8a,b to be less obvious than that at higher frequencies. At high wind, the differences of spectral slopes between biased and unbiased measurements are similar; see Fig. 8c. This indicates

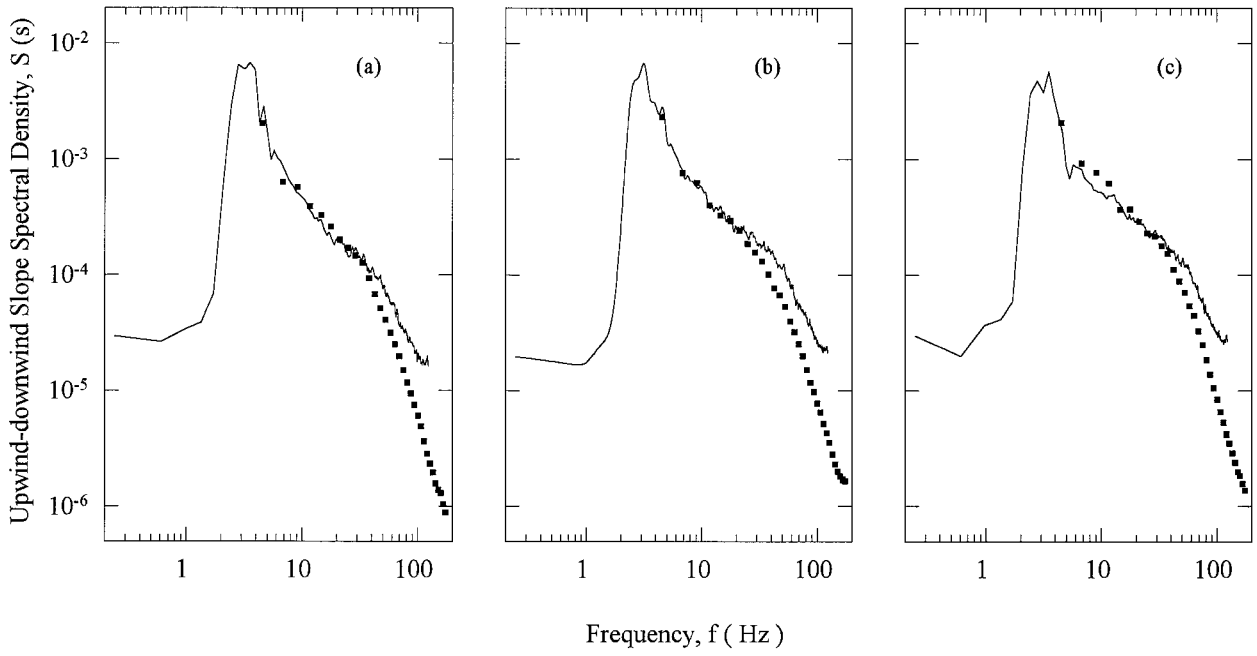

FIG. 9. Rain intensity influence on biased (■) and unbiased (–) frequency slope spectra. The result correspond to wind velocity of 5 m s^{-1} and rain intensities of (a) 42, (b) 68, and (c) 115 mm h^{-1}.

that the Doppler effect in these two regions are comparable. Essentially, the Doppler effects displayed by the spectra comes from the differences between the intrinsic and apparent wave frequencies. As noted above, these differences are due to wind-induced drift currents and long-wave orbital motions. Since the wind-induced drift currents are in the same direction as the wave propagation, the apparent (observed) frequency is higher than the intrinsic frequency. On the other hand, long-wave orbital motions introduce flow either along or against the ripple propagation. This may lead the shift of apparent frequency of ripples toward both higher and lower values. The existence of the transition frequency on the spectra reveals a balance between these two effects. Definitely the magnitudes of both wind-induced drift currents and long-wave orbital velocities are modulated by nonlinear interactions between different wave components.

It should be noted that, according to Hammack and Henderson (1993), the frequency of 19.6 Hz happens to be the transition point of the capillary–gravity and capillary waves, which is classified in terms of the frequency and the dimensionless surface tension based on weakly nonlinear wave train instability. The resonant quartets dominate the wave–wave resonant interaction at lower frequencies relative to the transition frequency, while the resonant triads dominate the interaction at higher frequencies. We speculate that the existence of the transition frequency is closely related to the wave–wave resonant interaction.

The Doppler effect at various rain intensities are shown in Fig. 9 ($U = 5$ m s^{-1}). The transition frequency is not affected by rain and is independent of the rain intensity. It remains at 19.6 Hz. Generally speaking, the Doppler effect is more obvious at high rain intensity than the medium and low rain intensities. This may be due to the fact that the intensity of enhancement on the surface currents and orbital motions from the rain-induced tangential stress is stronger at higher rain intensities.

c. Implications to oceanic remote sensing

Most oceanic remote sensing instruments receive their signals from the sea surface features. The combination of rain and wind effects impacts both scatterometry retrieval of sea surface winds and radar measurements of rainfall (Atlas 1994). According to our knowledge, Moore et al. (1979) and Bliven and Giovanageli (1993) reported the most representative radar work of rain effects on surface waves. Using an FM radar, Moore et al. (1979) performed laboratory backscatter measurements on rain effects at 14 GHz (22-mm wavelength) at an incidence angle of 40°. Except for one very high rain situation, their results indicate that at a given wind velocity the degree of enhancement is not consistently proportional to the rain intensity. The dependence of enhancement on the rain intensity varies with the wind velocity. This is similar to the present results, though the concrete variation patterns are different. Bliven and Giovanageli (1993) conducted their measurements in a wind–wave tank with a 36-GHz (18.3-mm wavelength) scatterometer operated at a 30° incidence angle. Their results show that at a given wind

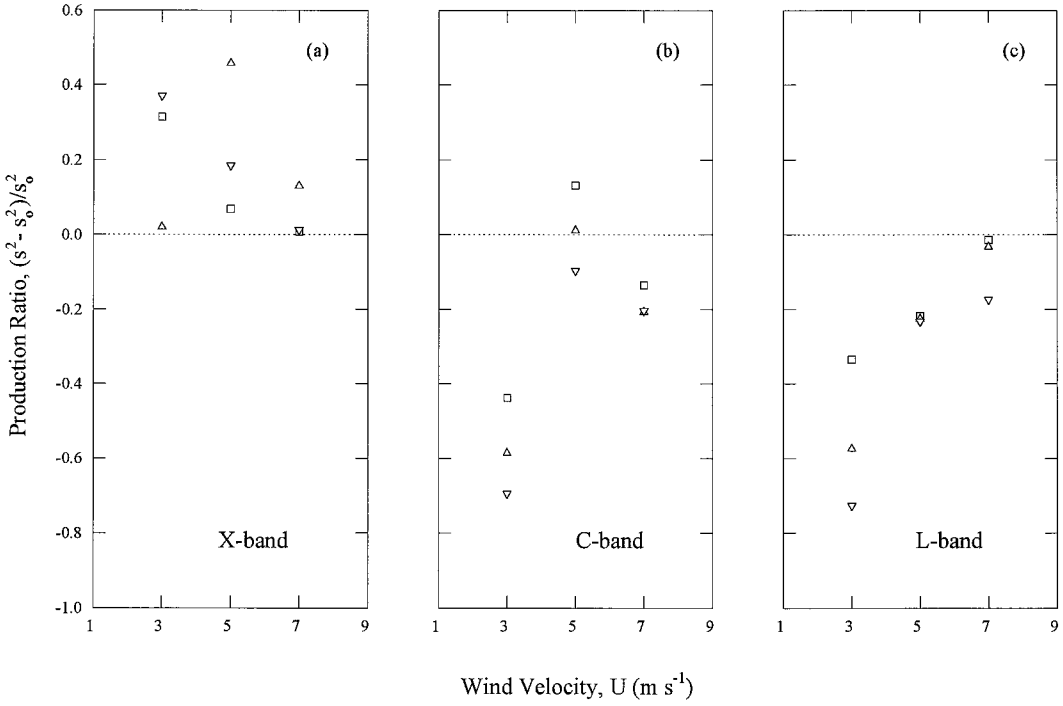

FIG. 10. Production ratios of surface roughness for X-, C-, L-band radars at 45° incidence angle. The rain intensities are 42 (□), 68(△), and 115 (▽) mm h^{-1}.

velocity, the rain enhancement on the surface roughness is in concert with the rain intensity. They found that radar returns from the disturbed water surface increased with the increasing rain intensity, indicating that the enhancement of surface roughness is proportional to the rain intensity.

Considering also dual effects of rain on the sea surface roughness discussed in the previous sections, it is beneficial to further estimate such effects on the surface roughness at several popular radar wavelength bands. Given the X-, L-, and C-band radars operated in the Bragg regime, the rain effects on the waves of $\lambda = 2.3$, 10 and 23 cm are shown in Fig. 10. In the figure, rain effects are expressed as the production ratio of surface roughness in terms of mean-square slopes. They are obtained from the wavenumber spectra shown in Fig. 5. Generally speaking, rain effects decrease with increasing wind speed all across three microwave bands. At high winds, there appears to be no obvious rain effects. This is consistent with previous results of rain effects on radar backscattering (Moore et al. 1979; Bliven and Giovanageli 1993). It suggests that during scatterometry retrieval of the wind vector, there is less need to modify the rain effects at high wind speed than for low wind situations, as indicated by Moore et al. (1979) and Bliven and Giovanageli (1993). This appears most obviously in the X-band. It is noted that, at a given wind speed, the production ratio shows different dependencies on the rain intensity in various radar bands. In the X-band, surface roughness is enhanced by rain, but the enhancement is not in concert with the rain intensity. This is qualitatively consistent with Moore et al.'s results, but different from those of Bliven and Giovanageli. For the C- and L-bands, the production ratios display approximately unique damping effects on the surface roughness except for one case in the C-band at $U = 5$ m s^{-1}. Generally speaking, for all three wind speeds, damping effects increase monotonically with increasing wind speed, but some differences still exist between production ratios in the C- and L-band. In the C-band, at moderate wind the damping effect appears weakest, and even some enhancement at light rain, while the weakest damping for the L-band occurs at high wind.

5. Concluding remarks

Effects of rain on sea surface roughness have been successfully investigated in the spatial domain. Complete descriptions of spectral properties under various wind speeds and rain intensities are obtained. The dual effects of rain, that is, damping and enhancement of the surface roughness, are clearly identified through unbiased measurements. Some subtle features of rain effects on the surface roughness are revealed: dual effects exist even in sole capillary–gravity/capillary region at some wind conditions. Damping or enhancement of the surface roughness by rain is shown at various wavenumber bands and depends on both wind and rain conditions.

Rain effects on the Doppler-shifted frequency of ripples are investigated by comparing the frequency slope

spectra both from biased and unbiased measurements. For a given wind speed, the Doppler effect increases with increasing rain intensity. The Doppler effect becomes more significant with increasing rain intensity. The Doppler effect is not observed at 19.6 Hz. It may be associated with resonant interactions among wave components. The overall rain effect on surface roughness is most significant at low winds. The results also shed light on the potential use of radar for the rain-cell detection. The choice of radar wavelength band in oceanic remote sensing in the presence of rain is also noted.

Numerous laboratory experiments have been conducted to investigate rain effects on surface waves. They have shown, at least qualitatively, the essential rain–wave interaction mechanisms. It is recognized that rain effects on water surface configuration depend on rain intensity, raindrop size, terminal velocity, and incident angle. Variation ranges of the first two factors are covered by previous simulations (Atlas 1994). Terminal velocity has not been achieved in the reported laboratory experiments. This may result in less severe damping on gravity waves. As another important property, wind-speed-dependent incident angle determines the partitioning of the raindrop momentum flux between its horizontal and vertical components and, hence, the net rain effects. Only rain effects at zero or moderate angle have been measured, while those of large angle at high wind speed are not known. Therefore, further studies on simulating the raindrop terminal velocity and high wind are suggested. During rain–wave interaction, different mechanisms due to various rain properties are coupled to generate the net rain effects. Except for a few case discussions (Bliven and Giovangeli 1993), they are investigated separately. Further studies on coupling processes are also suggested.

Acknowledgments. The authors appreciate the support of the Ocean Dynamics Program, National Aeronautics and Space Administration under Grant NAGW-2981 and the Remote Sensing Program, Office of Naval Research under Grants N00014-89-J-3226 and N00014-93-1-0345.

REFERENCES

Atlas, D., 1994: Footprints of storms on the sea: A view from spaceborne synthetic aperture radar. *J. Geophys. Res.*, **99,** 7961–7969.

Banner, M. L., I. S. F. Jones, and J. C. Trinder, 1989: Wavenumber spectra of short gravity waves. *J. Fluid Mech.,* **198,** 321–344.

Blackman, R. B., and J. W. Tukey, 1958: *The Measurement of Power Spectra.* Dover, 190 pp.

Bliven, L. F., and J. P. Giovanageli, 1993: An experimental study of microwave scattering from rain- and wind-roughened seas. *Int. J. Remote Sens.,* **14,** 855–869.

Caldwell, D. R., and W. P. Elliott, 1971: Surface stresses produced by rainfall. *J. Phys. Oceanogr.,* **1,** 145–148.

——, and ——, 1972: The effect of rainfall on the wind in the surface layer. *Bound.-Layer Meteor.,* **3,** 146–151.

Cataneo, R., and G. E. Stout, 1968: Raindrop-size distributions in humid continental climates and associated rainfall rate–radar reflectivity relationships. *J. Appl. Meteor.,* **7,** 901–907.

Dingle, A. N., and Y. Lee, 1972: Terminal fallspeeds of raindrops. *J. Appl. Meteor.,* **11,** 877–879.

Green, T., and D. F. Houk, 1979: The mixing of rain with near-surface water. *J. Fluid Mech.,* **90,** 569–588.

Hammack, J. L., and D. M. Henderson, 1993: Resonant interactions among surface water waves. *Annu. Rev. Fluid Mech.,* **25,** 55–97.

Hara, T., E. J. Bock, and D. Lyzenga, 1994: In situ measurements of capillary–gravity wave spectra using a scanning laser slope gauge and microwave radars. *J. Geophys. Res.,* **99,** 12 593–12 602.

Houk, D. F., and T. Green, 1976: A note on surface waves due to rain. *J. Geophys. Res.,* **81,** 4482–4484.

Katsaros, K., and J. K. Buettner, 1969: Influence of rainfall on temperature and salinity on the ocean surface. *J. Appl. Meteor.,* **8,** 15–18.

Le Méhauté, B., 1988: Gravity–capillary rings generated by water drops. *J. Fluid Mech.,* **197,** 415–427.

——, and T. Khangaonkar, 1990: Dynamic interaction of intense rain with water waves. *J. Phys. Oceanogr.,* **20,** 1805–1812.

Li, Q., M. Zhao, S. Tang, S. Sun, and J. Wu, 1993: Two-dimensional scanning laser slope gauge: Measurements of ocean-ripple structures. *Appl. Opt.,* **32,** 4590–4597.

Manton, M. J., 1973: On the attenuation of sea waves by rain. *Geophys. Fluid Dyn.,* **5,** 249–260.

Mitsuyasu, H., 1977: Measurement of the high-frequency spectra of ocean surface waves. *J. Phys. Oceanogr.,* **7,** 185–198.

Moore, R. K., Y. S. Yu, A. K. Fung, D. Kaneko, G. J. Dome, and R. E. Werp, 1979: Preliminary study of rain effects on radar scattering from water surface. *IEEE J. Oceanic Eng.,* **OE-4,** 31–32.

Phillips, O. M., 1977: *The Dynamics of the Upper Ocean.* 2d ed. Cambridge University Press, 336 pp.

Poon, Y.-K., S. Tang, and J. Wu, 1992: Interactions between wind and waves. *J. Phys. Oceanogr.,* **22,** 977–987.

Reynolds, O., 1900: On the action of rain to calm the sea. *Papers on Mechanical and Physical Subjects,* Vol. 1, Cambridge University Press, 86–88.

Tang, S., and J. Wu, 1992: Suppression of wind-generated ripples by surface films: A laboratory study. *J. Geophys. Res.,* **97,** 5301–5306.

Tsimplis, M., 1992: The effect of rain in calming the sea. *J. Phys. Oceanogr.,* **22,** 404–412.

——, and S. A. Thorpe, 1989: Wave damping by rain. *Nature,* **342,** 893–895.

van Dorn, W. G., 1953: Wind stress on an artificial pond. *J. Mar. Res.,* **12,** 249–276.

Willis, P. T., and P. Tattelman, 1989: Drop size distributions associated with intense rainfall. *J. Appl. Meteor.,* **28,** 3–15.

Wu, J., 1975: Wind-induced drift currents. *J. Fluid Mech.,* **68,** 49–70.

——, 1977: Directional slope and curvature distributions of wind waves. *J. Fluid Mech.,* **79,** 463–480.

——, 1986: Roughness elements of the sea surface, their spectral composition. *Tellus,* **38,** 178–188.

——, 1990: Mean-square slopes of the wind-disturbed water surface, their magnitude, directionality and composition. *Radio Sci.,* **25,** 37–48.

Zhang, X., 1994: Wavenumber spectrum of very short wind waves: An application of two-dimensional Slepian windows to the spectral estimation. *J. Atmos. Oceanic Technol.,* **11,** 489–505.

——, 1995: Capillary–gravity and capillary waves generated in a wind wave tank: Observations and theories. *J. Fluid Mech.,* **289,** 51–82.